Journal of Alloys and Compounds 803 (2019) 1054–1062

Contents lists available at ScienceDirect

Journal of Alloys and Compounds

journal homepage: http://www.elsevier.com/locate/jalcom

Applying a machine learning interatomic potential to unravel the effects of local lattice distortion on the elastic properties of multi-principal element alloys

Mehdi Jafary-Zadeh [a, *], Khoong Hong Khoo [a], Robert Laskowski [a], Paulo S. Branicio [b], Alexander V. Shapeev [c, **]

[a] Department of Materials Science and Chemistry, Institute of High Performance Computing (IHPC), A*STAR, Singapore 138632
[b] Mork Family Department of Chemical Engineering and Materials Science, University of Southern California, Los Angeles, CA, 90089-0241, USA
[c] Skolkovo Institute of Science and Technology, Skolkovo Innovation Center, Nobel Str. 3, Moscow, 143026, Russia

ARTICLE INFO

Article history:
Received 29 April 2019
Received in revised form
21 June 2019
Accepted 25 June 2019
Available online 26 June 2019

Keywords:
Multi-principal element alloys
High-entropy alloys
Elastic properties
Atomistic simulations
Machine learning

ABSTRACT

The concept of local lattice distortion (LLD) is of fundamental importance in the understanding of properties of high-entropy alloys and, more generally, of multi-principal element alloys (MPEAs). Despite previous experimental and computational efforts, the unambiguous evaluation of the static (due to atomic size difference) and dynamic (due to thermal fluctuation) LLD is still elusive. Here, as a first step, we develop a machine learning interatomic potential based on an efficient "learning-on-the-fly" scheme for CoFeNi, a prototypical ternary MPEA. Using this potential, we perform molecular dynamics simulations to calculate the elastic moduli of single- and polycrystalline CoFeNi. The results are in excellent agreement with theoretical and experimental data. As a second step, we design a simulation framework allowing the determination of the effects of static and dynamic LLD, thermal expansion, and chemical short-range order on the elastic properties of our prototypical MPEA. The results indicate that not only the average value of LLD, but also its probability distribution affect the elastic properties of MPEAs. In addition, we show that a variety of commonly used LLD indicators, *e.g.,* atomic strain, pair distribution function, and bond-length distribution, correlate with each other. Our results not only shed light on the of LLD in MPEAs, but also demonstrate the capabilities of our machine learning potential as a powerful tool for the development and characterization of novel alloys with designed properties.

1. Introduction

The traditional paradigm of alloy design (*i.e.* base-element approach) appears to have reached its limits to provide innovative alloys since no more stable metallic element remains to be used as the alloy base [1]. This limitation has inspired the emergence of high-entropy alloys (HEAs) or, more generally, multi-principal element alloys (MPEAs) [2,3]. According to the pioneering works of Yeh et al. [2] and Cantor et al. [3] the underlying design idea of these alloys was based on either increasing the configurational entropy of the mixture, to avoid the formation of undesirable intermetallic compounds [2], or exploring the central regions of phase diagrams [3]. HEAs/MPEAs were shown to exhibit exceptional functional and mechanical properties such as high specific strength [4], high ductility and attractive magnetic properties [5,6]. Particularly these alloys are promising for structural applications at harsh conditions such as cryogenic toughness, and high temperature strength and oxidation resistance [7–12]. Moreover, they offer a path to address the long-lasting strength-ductility paradox in metallurgy [9,10,13], by allowing simultaneous increase in strength and ductility [9,10].

Early works on HEAs [14], attributed the origin of their structure (mainly consisting of a random solid solution) and their exceptional properties to four hypothetical "core effects": (i) high-entropy (which motivated the HEA concept name); (ii) severe lattice distortion; (iii) sluggish diffusion; and (iv) the *cocktail* effect. Nevertheless, the wealth of emerging new data has recently led to open debates regarding the importance of these hypothetical core

* Corresponding author.
** Corresponding author.
E-mail addresses: zadehmj@ihpc.a-star.edu.sg (M. Jafary-Zadeh), a.shapeev@skoltech.ru (A.V. Shapeev).

https://doi.org/10.1016/j.jallcom.2019.06.318
0925-8388/

effects [15]. For instance, while numerous complex HEAs, containing 5 or more constituent elements, form two or more phases [16], simpler ternary and quaternary MPEAs, *e.g.* CoFeNi, CoCrNi, CoFeNiPd, NbMoTaW, *etc.*, form a single-phase random solid solution [7,17–21]. It is noteworthy that the highest fracture toughness at cryogenic temperatures among all metal alloys belongs to the CoCrNi alloy [20], which was attributed to the very low stacking fault energy in this ternary MPEA [22]. This result, has motivated an emerging trend to focus on the foundations of the structure-property relationships in MPEAs, also called complex concentrated alloys, which have a broader definition than HEAs [1]. In this work, we focus on the important and still not well understood effect of local lattice distortion (LLD) on the elastic properties of MPEAs.

The lattice distortion hypothesis postulates that different atomic radii of the constituent elements in MPEAs could lead to high levels of local (atomic level) distortions in the crystalline lattice [23]. It has been suggested that a variety of important physical and mechanical properties of HEAs are caused by their large lattice strains, including: low electrical and thermal conductivity and small temperature dependence of these properties [14,24], solid solution strengthening [25], etc. However, the nature of the HEA structure poses a challenge to the conventional experimental efforts to unambiguously characterize the extent of LLD in these alloys [26]. Recent diffraction results have suggested that the width of diffraction peaks of HEAs are not considerably larger than those in conventional alloys, and the effects of thermal fluctuations must be considered in the evaluation of LLD in these alloys [26]. Such observations indicate the importance of understanding both the *static LLD* (associated with different atomic sizes) vs. *dynamic LLD* (associated with thermal fluctuations) to shed light on the structure-property relations in MPEAs [27]. Nonetheless, a universal definition and quantification of static LLD in MPEAs still remains a challenge [26,27].

In conventional alloys, mean-field approaches, *e.g.* based on the classic Eshelby theory [28], have been widely employed to determine the local strain field around solvent atoms. However, the definition of solvent and solute atoms in MPEAs is irrelevant, precluding the use of such approaches. Alternatively, the magnitude of lattice distortion in MPEAs has been evaluated by the atomic size mismatch parameter, δ, based on the radii of the constituent atomic species, which is defined as [29–32]:

$$\delta = \sqrt{\sum_{i=1}^{N} c_i(1 - r_i/\bar{r})^2} \times 100, \quad (1)$$

where N is the number of elements, c_i and r_i are the atomic fraction and radius of the ith element, respectively, and $\bar{r}$ is the average atomic radius: $\bar{r} = \sum_{i=1}^{N} c_i r_i$. Nonetheless, this assessment can be ambiguous and inaccurate since atomic radii have different definitions, and they vary depending on the chemical environment of the atoms [23,33]. On the other hand, δ is merely evaluated based on the chemical composition; hence, it is not able to distinguish the static and dynamic lattice distortions for a given alloy. To have an accurate description of LLD in MPEAs, quantum mechanical (QM) calculations based on the density functional theory (DFT) have been employed to explicitly investigate the lattice distortion of HEAs/MPEAs [23,34]. For example, using DFT, researchers have proposed a model to calculate the LLD by taking into account both volumetric and shear atomic strains [34]. Since DFT simulations essentially offer the ground state configuration of the alloy, *i.e.* the structure at the absolute zero temperature, they can be used to evaluate the static LLD. QM-based (*ab initio*) molecular dynamics (MD) simulations could be used for that purpose though they tend to be computationally very expensive for systems larger than 100 atoms. On the other hand, large-scale MD simulations can be performed conveniently, if a high quality empirical or semi-empirical potential is available. Unfortunately, however, interatomic potentials are currently scarce for complex MPEA systems.

To enable MD simulations with the accuracy of quantum-mechanical (QM) calculations, a new generation of machine-learning (ML)-based approaches have recently emerged [35–45]. The key idea is to develop machine-interatomic potentials which map a set of atomic environments onto the numerical values of energies, forces, stresses, *etc.*, obtained from QM calculations. In contrast to empirical or semi-empirical interatomic potentials, based on relatively simple analytical functional forms, machine learning potentials (MLP) have a rather complex and flexible functional form as a function of the atomic position and chemical environment [38,46]. The functional form of MLPs typically contains hundreds of parameters "*learned*" (in a machine-learning sense) from a set of high-fidelity QM calculated data, referred to as the training data. Consequently, the trained MLP is a surrogate model interpolating the training data, and hence by orders of magnitude increases the efficiency of subsequent calculations of energies, forces, and stresses [47]. Such machine learning-based scheme was shown to exhibit superior accuracy as compared to conventional interatomic potentials for a variety of metallic and non-metallic materials [48–50] including phase stability and martensitic transition in metals [37,49].

In the current work, first we develop a moment tensor potential (MTP) [38,45–47] which is a class of machine learning potentials, for a prototypical MPEA, the CoFeNi alloy. MTP has been successfully applied to study single-component systems [51,52], single-phase binary systems [53], organic chemistry [54], and zero-temperature binary and ternary alloy structures [47]. The MTP potential allows for the "*learning on-the-fly*" scheme which offers a superior efficiency, by reducing the number of QM calculations, than classical potential trainings based on the *"learning and forgetting*" scheme [35,37,49]. The selected CoFeNi alloy is an important prototypical MPEA due to its promising structural and functional properties. Ni, Co, and Fe are the base elements of the major classes of conventional high temperature superalloys. Hence, CoFeNi is a fundamental base-MPEA to develop a new generation of superalloys, *i.e.* high entropy superalloys [55]. Moreover, this alloy system exhibits ultra-high magnetic saturation, electrical resistivity, mechanical malleability, superplasticity and shape memory effect [17,56–58]. After training the MTP, we use it to calculate the elastic moduli of the alloy. We further use the MTP to design a systematic MD framework to determine the effects of static and dynamic LLD on the elastic moduli of our prototypical MPEA. The effect of formation of chemical short-range order on the elastic properties of CoFeNi is also studied.

2. Methodology and simulation details

In this section, first we explain the setup of our quantum mechanical calculations based on which we trained our machine learning potential and evaluated it. We also describe the setup of our MD simulations and the framework we use to determine the effects of static and dynamic LLD on the elastic properties of the alloy. We also discuss the methodology we use to train our potential *on-the-fly* for the CoFeNi alloy.

2.1. Quantum-mechanical calculations

We perform quantum mechanical calculations in the framework of spin-polarized density functional theory (DFT) using the VASP package with the pseudopotentials treated using the projector

augmented-wave method [59,60]. A plane-wave energy cutoff of 300 eV is used for all calculations and the exchange-correlation potential is evaluated using the Perdew, Burke, and Ernzerhof implementation of the Generalized Gradient Approximation [61]. Structural optimization is carried out with a force tolerance of 0.01 eV/Å, and the Brillouin zone for our 108 atoms simulation cell is sampled with $6 \times 6 \times 6$ Monkhorst-Pack grid [62].

In our calculations, we first study the total energy as a function of lattice constant of the random structures of the alloys in a face-centered cubic (FCC) supercells containing 108 atoms. Atomic positions are relaxed while lattice constants are kept fixed and the optimal cell sizes fall in the range from 10.64 to 10.66 Å. The elastic constants C_{11}, C_{12} and C_{44} are then computed using the energy approach as described by Jamal et al. [63]. In this method, we apply various distortions on the previously relaxed unit cells and re-optimized the atomic positions while keeping the cell dimensions fixed. The total energies from these calculations are then substituted into a second order Taylor series expansion of total energy with respect to strains to evaluate the elastic constants. More specifically, we applied two cubic strains with $\varepsilon = 0.005$ and 0.01, as well as a monoclinic strain of $\varepsilon = 0.01$, and a tetragonal strain of $\varepsilon = 0.005$.

2.2. Molecular dynamics (MD) simulations

The Large-scale Atomic/Molecular Massively Parallel Simulator (LAMMPS) package is used to perform MD simulations [64,65]. The interactions between atoms in the CoFeNi alloy are modelled by the MTP as trained on-the-fly (see Sections 2.3 and 2.4 for details). To evaluate the precision of the trained MTP, we construct two series (containing either 108 or 4000 atoms) of 100 independent nominal equiatomic CoFeNi systems. In each system, the constituent elements are randomly distributed at the face-centered cubic (FCC) lattice points. The average atomic concentration (for Co, Fe and Ni) in these independent systems is ~33.3 at%, whereas its standard deviation is about 0.73 at% and 4.6 at% for the system of 4000 and 108 atoms, respectively. Here, we note that to model the structure of MPEAs, the special quasirandom structures (SQS) technique is alternatively used to optimize the computationally intensive first-principles calculations [23]. The three independent single-crystal elastic constants, *i.e.* C_{11}, C_{12}, and C_{44}, for the FCC lattice are calculated following the standard molecular dynamics methodology as in Ref. [66]. The elastic properties are calculated for all 100 systems and then averaged.

To setup a large-scale MD framework, an initial structure with FCC lattice and the ground state lattice parameter of 3.555 Å consisting of 10,976 atoms with a random distribution of equiatomic Co, Fe, Ni elements is constructed. For the melting-quenching simulations, the sample is first melted by thermalizing at 2300 K for 10 ns. Then, the liquid is quenched to room temperature (300 K) with a cooling rate of 1×10^{11} K/s, and equilibrated at 300 K for 5 ns. Periodic boundary conditions (PBCs) are applied in all three directions (x, y and z) of the simulation box to represent the bulk material. We design a heterogeneous crystallization by introducing a pre-existing FCC solid seed by freezing 0.5% of the total atoms at the centre of the simulation box. This solid seed provides a preferential site to facilitate the nucleation and growth of the desired FCC structure during the solidification process [67]. The isothermal–isobaric ensemble (NPT) is applied during the melting and quenching processes at zero pressure. In this ensemble, the temperature and pressure of the systems are controlled using a Nose-Hoover thermostat/barostat [68]. The Newtonian equations of motions are integrated with a time step of 2 fs employing the velocity Verlet algorithm. The OVITO package is used for visualization [69].

2.3. Machine-learning potential

We chose the MTP potential among the available catagories of machine-learning potentials [70]. MTP, akin to most interatomic potentials, assumes partitioning of the total interatomic interaction energy into individual contributions of each atom. These contributions depend on local atomic environments—mutual arrangements of atoms within the cut off sphere of the central atom. For the purpose of expressing the dependence of the energy on the atomic environments, the latter are described with moment tensor descriptors encoding the content of different shells of atoms around the central atom with moment of inertia tensors [70,71]. All contractions of these moment tensors satisfy all the needed physical symmetries and hence form a basis of a linear combination that is defined as the MTP energy. It has been shown mathematically that MTPs can approximate any local interatomic interaction to an arbitrary precision through increasing the number of approximation parameters [70,71]. The reader is referred elsewhere [72] for a detailed discussion on atomic environment descriptors and basis for expansion of interatomic potentials.

2.4. Learning-on-the-fly

We trained our machine learning potential, based on the "learning-on-the-fly" (LOTF) scheme [38,47]. In the LOTF scheme, essentially, the tuning of the parameters of the potential is actively performed during a molecular dynamics simulation and updating the training configurations by quantum mechanical calculations whenever is needed. While the MD simulation is running, the machine learning algorithm uses a "query strategy"—an algorithm of geometrically comparing a given configuration with the training configurations—to determine if the computed atomic configuration is sufficiently new to be added to the training set. If it needs to be added then the algorithm fetches the quantum mechanical (QM) calculations for this new configuration and adjusts the MTP parameters based on the obtained atomic energies, forces, and stresses. Indeed, the LOTF algorithm bridges the molecular dynamics driver (as implemented in LAMMPS) with a quantum mechanical model (in our case, VASP). The process of LOTF will be continued until the MTP stops seeing new configurations during the MD. The training efficiency and precision of the resulted MTP are determined by the extrapolation threshold, γ_{tsh}, which is, essentially, the tolerance above which a configuration is considered *sufficiently* new [38,47].

According to our LOTF scheme, the interatomic potential was trained using a dataset of 414 different atomic configurations (snapshots) selected during 100 independent molecular dynamics (MD) simulations such as melting and quenching. The initial supercell for each of these simulations was consisted of up to 74 atoms randomly distributed in different lattice structures, *i.e.* face centered cubic (FCC), body centered cubic (BCC), and hexagonal close pack (HCP). The MD scenarios included simulated melting-quenching and mechanical shearing processes. For the melting-quenching simulation, we melt the systems at 2300 K, thermalize it, and quench it to the room temperature with the cooling rate of 10^{13} K/s. Concerning mechanical shearing, we apply shear strain on the systems following a similar procedure as used for the calculation of generalized stacking fault energy of metals [73,74]. The DFT calculations are performed following the methodology explained in Section 2.1. The LOTF algorithm is based on evaluating extrapolation grades of atomic neighborhoods as the extent to which the configurations are new [38,47], and a threshold of $\gamma_{tsh} = 2$ which has been found to be sufficient for a variety of systems including multicomponent alloys [47,51,70].

3. Results and discussion

The elastic properties of alloys directly connect the interatomic interactions in their crystal structures to their stability. There are three independent second order single crystal elastic constants for a cubic lattice such as FCC, *i.e.*, C_{11}, C_{12}, and C_{44}. We calculated these elastic constants for our prototypical MPEA using the trained MTP and compared the results with those of DFT calculations. The results are shown in Fig. 1. The MTP results are calculated for the systems containing 108 and 4000 atoms by averaging over 100 independent configurations of randomly distributed Co, Fe and Ni elements with the nominal concentration of 33.3% each. The DFT results are calculated for the systems containing 108 atoms by averaging over 10 independent configurations. Fig. 1 indicates that the MTP is able to predict the elastic properties of the CoFeNi alloy with first-principles accuracy.

Based on the single-crystal elastic constants, we also calculate the polycrystalline Young's modulus, *E*, bulk modulus, *B*, and shear modulus, *G* of the CoFeNi alloy by using the Voigt-Reuss-Hill averaging method [75,76]. The values of the equilibrium lattice parameter, *a*, single-crystal elastic constants, and polycrystalline elastic moduli are presented in Table 1. Other theoretical and experimental values available in the literature are also shown for reference in this table. From Table 1, it can be seen that the ground state lattice parameter (at 0 K) of the FCC CoFeNi alloy is about 3.555 Å (calculated for the system of 4000 atoms using MLP). This value is in excellent agreement both with our other calculations using MLP and DFT in the smaller systems containing 108 atoms, and other theoretical calculations (*e.g.* 3.559 Å [23], 3.545 Å [77]). The smaller value of our lattice parameter compared to the experimental values is due to the effect of thermal expansion at room temperature measurements, which will be discussed in the next sections. Furthermore, Table 1 indicates that the rules for dynamical (mechanical) lattice stability [78,79] are satisfied for the FCC CoFeNi alloy: $C_{44} > 0$, $C' = (C_{11} - C_{12})/2 > 0$, and $B > 0$. Overall, our MTP-based calculations are in good agreement with other theoretical and experimental reports. It is noteworthy that our potential has not been fitted to any experimental or theoretical lattice properties such as lattice parameters, elastic constants, *etc*. Hence, our results demonstrate the strength of our machine learning technique to develop accurate interatomic potentials for complex alloys.

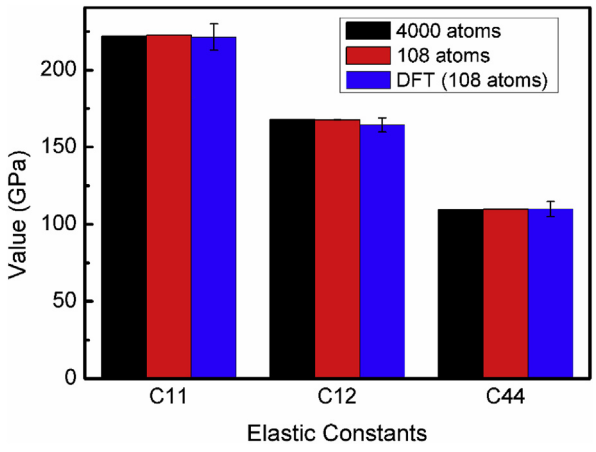

Fig. 1. Calculated single crystal elastic constants for the CoFeNi alloy with cubic (FCC) structure. The red and black bars show the results by using the MTP machine learning interatomic potential for simulation systems with 108 and 4000 atoms, respectively. The values are averaged over 100 different atomic configurations with nominal equi-atomic chemical compositions. Elastic constants calculated using DFT for 108 atoms (averaged over 10 configurations) are also shown in blue bars. (For interpretation of the references to colour in this figure legend, the reader is referred to the Web version of this article.)

After having established that our machine learning potential could successfully predict the elastic moduli of CoFeNi MPEA, we apply it to run MD simulations to determine and discriminate between the effects of static and dynamic LLD on the elastic properties of the material. We consider 5 different system states as summarized in Table 2. Our system of equiatomic CoFeNi alloy contains 10,976 atoms of randomly distributed constituent elements. In State 1, *i.e.* "*pristine*" state, the atoms are located at the ideal points of an FCC lattice with the ground state (effective) lattice parameter of 3.555 Å as obtained by fully relaxing the simulation box while keeping the fractional coordinates fixed. This configuration implies the absence of any lattice distortion in State 1. To obtain State 2, we relaxed the atomic structure and simulation box of the State 1. During the structural relaxation, the atoms displace away from their ideal lattice positions leading to local distortions (strains) in the perfect FCC lattice. Such a local distortion/strain for an individual atom is referred to as static LLD [27]. The magnitude of this local distortion depends on the atom's type, volume, and chemical environment. Indeed, State 2 introduces the "static" LLD into the pristine structure (State 1). Here, it is noteworthy that even after relaxation of the simulation box of State 1 (to obtain State 2), the effective lattice parameter of the system is 3.555 Å demonstrating that the static LLD does not affect the lattice parameter of the alloy.

To obtain State 3, we performed a melting-quenching simulation starting at State 2 (for more details see Section 2, "Methodology and simulation details"). In brief, we melt the system and equilibrate the liquid alloy at 2300 K. Then, we quenched the liquid to room temperature (300 K) to obtain the FCC solid solution. This process allows the atomic species to explore the potential energy landscape of the system and develop chemical short-range order (CSRO) whose extent depends on the chemical affinities of the constituent elements. It is noteworthy that formation of CSRO in high-entropy alloys and metallic glass systems has been studied [67,80]. In our framework, after we thermalize the solidified alloy at 300 K, we select an instantaneous state of the system as State 3. Hence, the structure of State 3 contains a combination of static LLD (associated with difference in atomic volumes), dynamic LLD (associated with the thermal oscillations of the atoms), thermal expansion (at room temperature), and possibly, formation of CSRO during the solidification. The crystal of a complex solid solution contains static LLD. Hence, the thermal oscillations occur around the displaced atomic positions instead of the ideal lattice points. To remove the dynamic LLD from State 3 and obtain State 4, we relaxed the atomic structure by keeping the simulation box fixed. In this case, the off-site displacement of the atoms due to thermal oscillations will be smeared out, while the simulation box is kept fixed, implying that the thermal expansion effect at room temperature is retained. Consequently, the structure of State 4 includes static LLD, thermal expansion and CSRO. Next, we further relaxed the simulation box of State 4 to remove the thermal expansion effect and gain the State 5 (equal to zero temperature structure). As a result, structure of State 5 contains the effects of static LLD and CSRO. The corresponding values of lattice parameter, *a* (Å), and elastic moduli (in GPa unit) of these five states are presented in Table 2. It is noteworthy that including the thermal expansion (at 300 K) in our atomistic model of the CoFeNi alloy (i.e. States 3 and 4) leads to a room temperature lattice parameter of 3.573 Å which is in excellent agreement with experimental measurements, 3.57–3.58 Å [17,81]. Here, we note that the elastic properties and lattice parameter of States 3 and 4 are calculated by time-averaging of the thermalized system at 300 K. Obtaining the shear, bulk and

Table 1
Evaluation of CoFeNi single-crystal and polycrystalline elastic properties calculated using MTP vs. results from experiments or first-principles calculations in the literature. The data include equilibrium lattice parameter (Å), single crystal elastic constants C_{11}, C_{12}, C_{14}, and $C'=(C_{11}-C_{12})/2$ (GPa), polycrystalline elastic properties according to Voigt-Reuss-Hill averaging, including sheer modulus G, bulk modulus B, Young's modulus E (GPa), Poisson's ratio ν, and B/G ratio. For our MTP calculations, we considered averaging the properties over 100 samples (consisted of either 4000 or 108 atoms in the supercell) with the nominal equi-molar composition of CoFeNi but different configuration of atomic species. For our DFT results, we similarly performed averaging over 10 supercells consisting of 108 atoms with nominal chemical composition of CoFeNi but different atomic configurations.

CoFeNi system	a	C_{11}	C_{12}	C_{44}	C'	G	B	E	ν	B/G
MTP (4000 atoms)	3.555	222.02	167.91	109.5	27.02	63.01	185.93	169.6	0.348	2.96
MTP (108 atoms)	3.553	222.67	167.7	109.8	27.49	63.39	186.02	170.73	0.347	2.92
DFT (108 atoms)`	3.554	221.45	166.31	109.9	27.74	63.52	184.7	170.95	0.345	2.89
Exp.[a]		–	–	–	–	60	180	162	0.35	3
Exp. (at 300 K/0 K)[b]	3.58/-	–	–	–	–	68/72	136/138	175/184	0.28	2.0/1.9
Exp.[c,d]	3.57[c]	–	–	–	–	–	–	162.0[d]	–	–
DFT (+exp. feet)[e]		205.1	148.7	135.0	28.2	73.0	167.5	191	0.310	2.29
DFT[f]	3.559	–	–	–	–	–	179.5	–	–	–
DFT (MaxEnt/SRO)[g]	3.545/3.543	243.6/244.8	155.3/156.6	130/132	45.1/44.1	84.5/85.1	184.7/186.0	219.8/221.5	0.302	2.19

[a] Ref. [95].
[b] Ref. [81]. The elastic properties at 0 K are obtained by fitting to experimental data at finite temperatures.
[c] Ref. [17].
[d] Ref. [96].
[e] Ref. [97].
[f] Ref. [23]. Using SQS technique.
[g] Ref. [77]. The MaxEnt results have been calculated using a SQS supercell of 108 atoms, and a combination of DFT and Monte Carlo techniques has been employed to calculations the SRO results.

Table 2
Effect of lattice distortion on elastic properties of the CoFeNi alloy. This table includes the values of lattice parameter (Å) and elastic moduli (GPa) calculated for different states of the CoFeNi alloy before and after a series of melting/quenching MTP-based MD simulation. The supercell contains 10,976 atoms (nominally 33.3 at% for each of the constituent elements). Table also explains the contribution of static and/or dynamic LLD in the overall LLD and other parameters (such as formation of CSRO, etc.) which could affect the elastic properties. Hence, the variation of elastic properties at these states could be attributed to the specific state of lattice distortions in the alloy structure.

Alloy State	Remarks	LLD & other effects included	a	G	B	E	ν
State 1	Pristine structure: atoms are located at the ideal FCC lattice points with the ground state lattice parameter	no LLD	3.555	63.87	187.4	172.07	0.347
State 2	Ground state structure: after relaxing the simulation box and atomic positions of State 1.	static LLD	3.555	62.88	185.68	169.51	0.348
State 3*	An instantaneous room temperature structure of the solidified alloy after a melting and quenching process.	static LLD + dynamic LLD + thermal expansion + CSRO	3.573	61.18	177.49	164.62	0.345
State 4*	Relaxing the atomic positions of State 3 within a fixed simulation box: In this case the thermal lattice fluctuations are removed, while the thermal expansion is preserved.	static LLD + thermal expansion + CSRO	3.573	62.43	184.54	168.30	0.349
State 5	Relaxing the simulation box of State 4: thermal expansion is removed.	static LLD + CSRO	3.558	62.40	184.53	168.24	0.348

Young's modulus for States 1 to 5 allows us to clearly evaluate the effects of static LLD, dynamic LLD, thermal expansion and CSRO on the elastic properties of our prototypical MPEA. To that end, we first discuss our methodology of evaluating the lattice distortion in the following.

To quantitatively characterize the LLD, we calculate the local (atomic) elastic strains based on the elastic deformation gradient tensor, F^e, which is related to the local gradient of the elastic displacements [82]. The F^e tensor transforms vectors from an imaginary ideal crystal (i.e. strain- and stress-free state) to a physical configuration of the crystal (such as a simulation snapshot to be analyzed), as the following:

$$\Delta x = F^e \cdot \Delta X, \tag{2}$$

Where ΔX is a vector in the ideal crystal lattice, i.e. the material frame, and Δx is the corresponding vector in the strained or distorted crystal. We use the OVITO package [69] to compute the local strain tensor at each atom by taking into account the atomic positions in the local neighborhood, *e.g.* 12 nearest-neighbors (NN) for the FCC lattice. Indeed, the calculated strain of an atom evaluates the extent of local distortion from the imaginary position of the atom in an ideal crystal lattice. Note that the calculated elastic strain tensor is composed of both shear and volumetric components. In this work, we use the volumetric component of the atomistic strain, ε_i^v, as the indicator of LLD for the ith atom in the system. This is reasonable since the volumetric strain of atoms can be directly related to other alternative LLD indicators such as atomic size, or the pair distribution functions (PDFs). Besides, the volumetric elastic strain of atoms have been used in the theoretical models of solid solution strengthening [32].

Based on the methodology explained above, we calculate the average atomic volumetric elastic strain in the system, $\overline{\varepsilon^v} = \sum_{i=1}^{N} \varepsilon_i^v / N$, where ε_i^v is the volumetric elastic strain of the ith atom and N is the number of atoms, for the five different states of the CoFeNi alloy (see Table 2). Fig. 2(a) shows the variations of $\overline{\varepsilon^v}$ and the corresponding elastic moduli for these states. It can be seen that the average elastic strain of pristine lattice in State 1 is zero. This indeed is expected since State 1 is an ideal FCC crystal with the lattice parameter of (ground state) 3.555 Å, and hence it is free of any local lattice distortion by default. More interestingly, the average of LLD in State 2, merely containing static LLD, is also zero while there are reductions in the elastic moduli as compared with State 1. This implies that while the static LLD does not have an overall effect on the macroscopic strain status of the alloys, it still affects the elastic properties of the material. States 3 and 4 have the

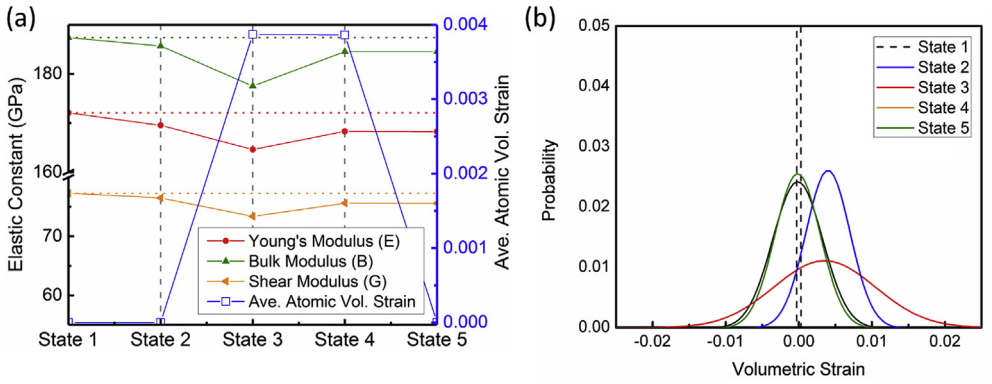

Fig. 2. Effects of lattice distortion on isotropic (polycrystalline) elastic moduli of the CoFeNi alloy. (a) The left axis presents the variation of elastic moduli (Young's modulus, *E*, bulk modulus, *B*, and shear modulus, *G*) at different states of the alloy (see Table 2 for details). The right axis presents the average of the local lattice distortion, as quantified by the average atomic volumetric elastic strain $\overline{\varepsilon^v} = \sum_{i=1}^{N} \varepsilon_i^v / N$, where ε_i^v is the volumetric strain of the *i*th atom and *N* is the number of atoms [82]. **(b)** The probability distribution of the LLD at different states of the system. Comparing (a) and (b) indicates that not only the average lattice distortion but also the details of the distribution of LLD affects the elastic properties of the MPEA.

highest (positive) level of $\overline{\varepsilon^v}$ which is contributing to the thermal expansion at room temperature. While the magnitude of $\overline{\varepsilon^v}$ in both of these states are equal, the elastic moduli of State 3 is the lowest among all states, which is attributed to the presence of dynamic LLD in State 3. Hence, the recovery of elastic moduli in State 4 (as compared with state 3) is due to the removal of thermal fluctuations from the crystal structure. State 5 exhibits further enhancement of elastic moduli which could be attributed to the removal of thermal expansion in this state.

According to the above, the variations in the elastic properties in Fig. 2(a) could be attributed to the atomistic structure of the CoFeNi alloy at different states (with presence/absence of static LLD, dynamic LLD, etc.). Nevertheless, $\overline{\varepsilon^v}$ alone is not able to explain these variations. Fig. 2(b) shows the probability distribution of the local volumetric strain, ε_i^v, for different states. The delta function (black dash-lines) at the volumetric strain of 0 indicates the pristine structure (State 1). It can be seen that introducing the static LLD in State 2 leads to widening of the ε_i^v distribution around the zero average. In both State 3 and State 4, thermal expansion leads to a positive shift in the distributions toward the average of ~0.004, which indeed is the value of $\overline{\varepsilon^v}$ for these states (see in Fig. 4(a)). However, the deviation in the probability distribution of ε_i^v of State

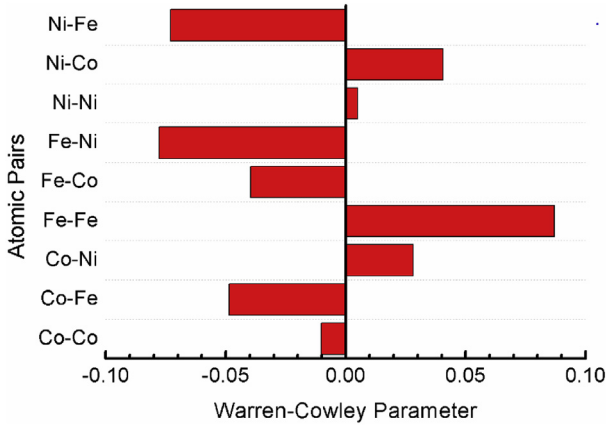

Fig. 4. Formation of CSRO in solidified CoFeNi. The Warren-Cowley parameter, α_{AB}, is calculated as an indicator of CSRO. $\alpha_{AB} < 0$: bond formation is favorable; $\alpha_{AB} > 0$: bonding is avoided; α_{AB} ~0: bond formation is random.

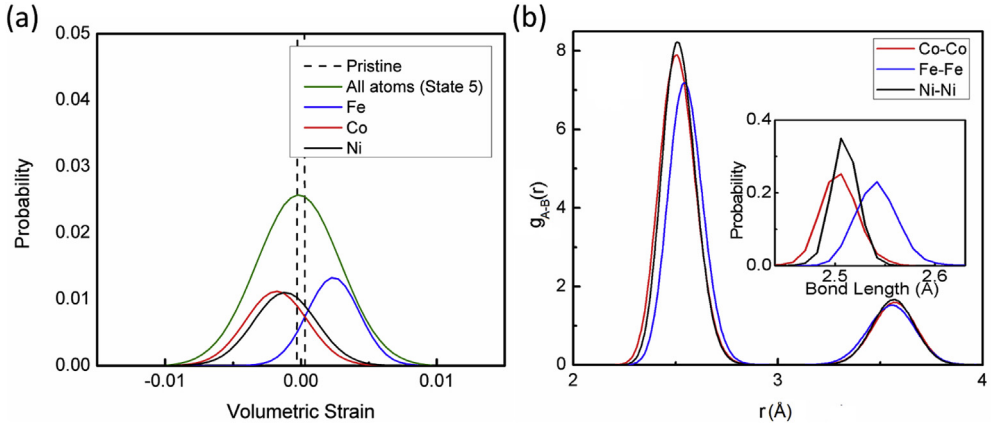

Fig. 3. Details of lattice distortion for different constituent elements in the CoFeNi Alloy (a) Overall and partial (for different constituent elements) distributions of local lattice distortion (in terms of volumetric strain) for the CoFeNi alloy at the State 5 (see Table 2 for details). **(b)** The partial pair distribution functions (PDFs), $g_{AB}(r)$, for Co–Co, Fe–Fe, and Ni–Ni pairs. It can be seen that the distance between Fe atoms at their nearest-neighbor (NN) shell is longer than the same distance between Co and Ni atoms, while the distance between Co atoms at the NN shell is the shortest. **(inset)** The distribution of bond lengths for Co, Fe, and Ni atoms with their similar species.

4 is markedly wider than that of State 3, which is attributed to the existence of thermal fluctuations (and hence the dynamic LLD) in State 4. Hence, it can be concluded that the lower values of elastic moduli in State 4 as compared with State 3 is attributed to the wider deviation its ε_i^v distribution.

Fig. 3(a) shows the overall (all-atoms) and the partial distribution of volumetric strain, ε_i^v, for the CoFeNi alloy at State 5. While the average value of all-atoms distribution of ε_i^v is zero, that of partial distribution of Fe (Co and Ni) have a shift toward positive (negative) values. This indicates that there is a volumetric expansion around the Fe atoms and volumetric shrinkage around the Co and Ni atoms.

Basically, the partial pair distribution function (PPDF), $g_{AB}(r)$, has been used to determine the probability of finding atoms of type *B* at a distance of *r* from a central atom of type *A*, normalized by their respective densities [83,84]:

$$g_{AB}(r) = \frac{1}{4\pi r^2 \rho_0 c_B} \frac{dn_{AB}}{dr}, \tag{3}$$

where, *r* is the distance, ρ_0 is the number density of all atoms, c_B is the fraction of type B atoms in the system, and $<dn_{AB}(r)>$ is the ensemble average of the number of atoms of type B existing between the distances of *r* and $r + dr$ from a type A atom. Fig. 3(b) shows the calculated *PPDF* for similar species of the CoFeNi MPEA, *i.e.* g_{AA}. According to this figure, the first peak of the PPDF (corresponding to the nearest-neighbor (NN) shell) for the Fe–Fe pair has a shift toward larger distance, *r*, while that of Co–Co and Ni–Ni has a shift toward shorter distances. The mismatches in the positions of the first peaks of these PPDFs are in agreement with the variations in the bond length of Fe–Fe (2.543 Å) Co–Co (2.503 Å) and Ni–Ni (2.508 Å) as presented in the inset of Fig. 3(b). A comparison of Fig. 2(a) and (b) suggests that the volumetric expansion (shrinkage) around Fe (Co and Ni) atoms can be attributed to the larger (shorter) bond lengths associated with these atomic species. Hence, we postulate that while a variety of LLD indicators have been proposed for MPEAs, *e.g.* pair distribution functions [85], bond-length distribution [23,86], volumetric/shear atomic strains [34], and atomic stresses [87], etc., these indicators might be inter-correlated. This implies the necessity of further investigations to evaluate such correlations and shed light on the structure-property relations in MPEAs.

It is generally believed that MPEA, in particular HEAs, are intrinsically random solid solutions. However, the diversity in the chemical affinity of multiple constituent elements in these alloys might lead to formation of microscopic chemical make-ups, *i.e.* chemical short-range order (CSRO), at the nearest-neighbor shell of atomic species [88,89]. Formation of CSRO in MPEAs affects their physical and mechanical properties [77,90] as well as their structural stability [89]. As a consequence, it has recently received considerable theoretical and experimental attention [88,89,91–93]. For example, experimental studies have provided evidence of CSRO in the CrCoNi alloy, in which the Cr atoms separate from each other, whereas they exhibit tendency to bond with Co and Ni atoms [93]. To quantitatively investigate the formation of CSRO in our CoFeNi alloy, we use the Warren-Cowley parameter (WCP) which is calculated for a given atomic pair, α_{AB}, as the following [84,94]:

$$\alpha_{AB} = 1 - \frac{Z_{AB}}{c_B Z_A}, \tag{4}$$

where Z_{AB} is the number (partial coordination number, CN) of atoms of type B at the nearest-neighbor shell of the atom of type *A*, Z_A is the total CN of atom *A*, c_B is the atomic fraction of type *B* in the alloy. $\alpha_{AB} < 0$ indicates that bond formation between *A* and *B* is favorable, $\alpha_{AB} > 0$ indicates that the bond formation is avoided, and if α_{AB} ~0, the bond formation is random.

Fig. 4 shows the values of the WCP for all possible pairs of atomic species in the CoFeNi alloy at State 5. We recall that State 5 is obtained through solidification and full structural relaxation processes (see Table 2). It can be seen that the values of the WCP for different atomic pairs in this alloy are around zero, in the range of about −0.08 to 0.09. According to this figure, since $\alpha_{Co\text{-}Co}$ and $\alpha_{Ni\text{-}Ni}$ are almost 0, either of the Co and Ni atoms are randomly distributed around the atoms of their own type. In contrast, the apparent positive value of $\alpha_{Fe\text{-}Fe}$ *~0.09* indicated that in this alloy, the Fe atoms separate from each other. Moreover, the distinct negative values of $\alpha_{Fe\text{-}Ni}$ and $\alpha_{Ni\text{-}Fe}$ demonstrate a higher chemical affinity between Fe and Ni species for bonding. As a conclusion and according to Table 2, the relatively small difference in the elastic properties of CoFeNi alloy between State 5 and State 2 (~0.7%) could be attributed to the formation of CSRO in State 5 during the solidification process. Here, it is noteworthy that according to recent studies, the extent of formation of CSRO in MPEAs is much smaller than that in metallic glasses, which is due to the closer chemical affinities (small mixing enthalpy) of the constituent elements in MPEAs as compared with the glass forming alloys [67]. Other theoretical studies also supports that formation of CSRO could slightly alter the elastic moduli (~0.5–0.7%) of the MPEAs [77]. Further research has demonstrated that CSRO could have significant effects on the intrinsic and extrinsic stacking fault energy of MPEAs, and hence their deformation mechanisms [90]. Hence, further comprehensive research is crucial to investigate the extent of short-range order in MPEAs and its relations with their properties.

4. Conclusions

We used an active learning approach to train an MTP, a type of a machine learning potential, for the CoFeNi alloy, an important prototypical MPEA. In contrast with empirical and semi-empirical potentials, the MTP was not explicitly fitted to lattice/bulk properties (such as lattice parameter, elastic constants, etc.). Nonetheless, we demonstrated that it is capable of predicting these properties in excellent agreement with quantum mechanical calculations and experiments. Based on our MTP, we performed a series of MD simulations to determine and discriminate the effects of static and dynamic LLD, thermal expansion and formation of CSRO on the elastic properties of MPEAs. We demonstrated that while the average of the static LLD in the material is zero (i.e. the material is overall strain free), it reduces the elastic moduli. The influence of the dynamic LLD on the elastic moduli is stronger than that of the static LLD. That could be attributed to its wider deviation of probability distribution. We further used our framework to determine the effects of thermal expansion and CSRO on the elastic properties. The lack of reliable and efficient interatomic potentials is a bottleneck in the discovery of novel alloys and the study of their structure-property relations. Here, we suggest a possible solution path by demonstrating our machine learning-based methodology as a powerful tool to perform high throughput calculations and explore the large compositional landscape of MPEAs.

Acknowledgements

The authors gratefully acknowledge the financial support from Agency for Science, Technology and Research (A*STAR), Singapore, and the use of computing resources provided by A*STAR Computational Resource Centre (A*CRC). A.V.S. acknowledges the support by the Russian Science Foundation (grant number 18-13-00479).

References

[1] S. Gorsse, J.-P. Couzinié, D.B. Miracle, From high-entropy alloys to complex concentrated alloys, Compt. Rendus Phys. 19 (2018) 721–736.
[2] J.-W. Yeh, S.-J. Lin, T.-S. Chin, J.-Y. Gan, S.-K. Chen, T.-T. Shun, C.-H. Tsau, S.-Y. Chou, Formation of simple crystal structures in Cu-Co-Ni-Cr-Al-Fe-Ti-V alloys with multiprincipal metallic elements, Metall. Mater. Trans. A 35 (2004) 2533–2536.
[3] B. Cantor, I. Chang, P. Knight, A. Vincent, Microstructural development in equiatomic multicomponent alloys, Mater. Sci. Eng. A 375 (2004) 213–218.
[4] E. Jumaev, S.H. Hong, J.T. Kim, H.J. Park, Y.S. Kim, S.C. Mun, J.-Y. Park, G. Song, J.K. Lee, B.H. Min, Chemical evolution-induced strengthening on AlCoCrNi dual-phase high-entropy alloy with high specific strength, J. Alloy. Comp. 777 (2019) 828–834.
[5] P. Li, A. Wang, C. Liu, A ductile high entropy alloy with attractive magnetic properties, J. Alloy. Comp. 694 (2017) 55–60.
[6] Z. Wu, C. Parish, H. Bei, Nano-twin mediated plasticity in carbon-containing FeNiCoCrMn high entropy alloys, J. Alloy. Comp. 647 (2015) 815–822.
[7] O. Senkov, G. Wilks, D. Miracle, C. Chuang, P. Liaw, Refractory high-entropy alloys, Intermetallics 18 (2010) 1758–1765.
[8] O. Senkov, G. Wilks, J. Scott, D. Miracle, Mechanical properties of $Nb_{25}Mo_{25}Ta_{25}W_{25}$ and $V_{20}Nb_{20}Mo_{20}Ta_{20}W_{20}$ refractory high entropy alloys, Intermetallics 19 (2011) 698–706.
[9] B. Gludovatz, A. Hohenwarter, D. Catoor, E.H. Chang, E.P. George, R.O. Ritchie, A fracture-resistant high-entropy alloy for cryogenic applications, Science 345 (2014) 1153–1158.
[10] T. Liu, Z. Wu, A. Stoica, Q. Xie, W. Wu, Y. Gao, H. Bei, K. An, Twinning-mediated work hardening and texture evolution in CrCoFeMnNi high entropy alloys at cryogenic temperature, Mater. Des. 131 (2017) 419–427.
[11] J. Chen, X. Zhou, W. Wang, B. Liu, Y. Lv, W. Yang, D. Xu, Y. Liu, A review on fundamental of high entropy alloys with promising high–temperature properties, J. Alloy. Comp. 760 (2018) 15–30.
[12] B. Gorr, M. Azim, H.-J. Christ, T. Mueller, D. Schliephake, M. Heilmaier, Phase equilibria, microstructure, and high temperature oxidation resistance of novel refractory high-entropy alloys, J. Alloy. Comp. 624 (2015) 270–278.
[13] Y.F. Ye, Q. Wang, J. Lu, C.T. Liu, Y. Yang, High-entropy alloy: challenges and prospects, Mater. Today 19 (2016) 349–362.
[14] Y. Jien-Wei, Recent progress in high entropy alloys, Ann. Chim. Sci. Mat 31 (2006) 633–648.
[15] D.B. Miracle, High entropy alloys: a current evaluation of founding ideas and core effects and exploring nonlinear alloys (postprint), JOM 69 (2017) 2130–2136.
[16] Z. Wang, S. Guo, C.T. Liu, Phase selection in high-entropy alloys: from nonequilibrium to equilibrium, JOM 66 (2014) 1966–1972.
[17] P. Li, A. Wang, C. Liu, Composition dependence of structure, physical and mechanical properties of FeCoNi (MnAl) x high entropy alloys, Intermetallics 87 (2017) 21–26.
[18] B. Gludovatz, A. Hohenwarter, K.V. Thurston, H. Bei, Z. Wu, E.P. George, R.O. Ritchie, Exceptional damage-tolerance of a medium-entropy alloy CrCoNi at cryogenic temperatures, Nat. Commun. 7 (2016) 10602.
[19] R. Kozak, A. Sologubenko, W. Steurer, Single-phase high-entropy alloys–an overview, Z. für Kristallogr. - Cryst. Mater. 230 (2015) 55–68.
[20] B. Gludovatz, A. Hohenwarter, K.V.S. Thurston, H. Bei, Z. Wu, E.P. George, R.O. Ritchie, Exceptional damage-tolerance of a medium-entropy alloy CrCoNi at cryogenic temperatures, Nat. Commun. 7 (2016) 10602.
[21] N. Gurao, K. Biswas, In the quest of single phase multi-component multi-principal high entropy alloys, J. Alloy. Comp. 697 (2017) 434–442.
[22] G. Laplanche, A. Kostka, C. Reinhart, J. Hunfeld, G. Eggeler, E.P. George, Reasons for the superior mechanical properties of medium-entropy CrCoNi compared to high-entropy CrMnFeCoNi, Acta Mater. 128 (2017) 292–303.
[23] H. Song, F. Tian, Q.-M. Hu, L. Vitos, Y. Wang, J. Shen, N. Chen, Local lattice distortion in high-entropy alloys, Phys. Rev.Mater. 1 (2017), 023404.
[24] J.-W. Yeh, Physical metallurgy of high-entropy alloys, JOM (J. Occup. Med.) 67 (2015) 2254–2261.
[25] F. Wang, Y. Zhang, G. Chen, Atomic packing efficiency and phase transition in a high entropy alloy, J. Alloy. Comp. 478 (2009) 321–324.
[26] L. Owen, E. Pickering, H. Playford, H.J. Stone, M. Tucker, N.G. Jones, An assessment of the lattice strain in the CrMnFeCoNi high-entropy alloy, Acta Mater. 122 (2017) 11–18.
[27] L.R. Owen, N.G. Jones, Lattice distortions in high-entropy alloys, J. Mater. Res. 33 (2018) 2954–2969.
[28] J. Eshelby, The continuum theory of lattice defects, in: Solid State Physics, Elsevier, 1956, pp. 79–144.
[29] S. Guo, C.T. Liu, Phase stability in high entropy alloys: formation of solid-solution phase or amorphous phase, Prog. Nat. Sci.: Mater.Int. 21 (2011) 433–446.
[30] Y. Zhang, Y.J. Zhou, J.P. Lin, G.L. Chen, P.K. Liaw, Solid-solution phase formation rules for multi-component alloys, Adv. Eng. Mater. 10 (2008) 534–538.
[31] T. Egami, W. Guo, P. Rack, T. Nagase, Irradiation resistance of multicomponent alloys, Metall. Mater. Trans. A 45 (2014) 180–183.
[32] Y.F. Ye, C.T. Liu, Y. Yang, A geometric model for intrinsic residual strain and phase stability in high entropy alloys, Acta Mater. 94 (2015) 152–161.
[33] V.A. Lubarda, On the effective lattice parameter of binary alloys, Mech. Mater. 35 (2003) 53–68.
[34] Y. Ye, Y. Zhang, Q. He, Y. Zhuang, S. Wang, S. Shi, A. Hu, J. Fan, Y. Yang, Atomic-scale distorted lattice in chemically disordered equimolar complex alloys, Acta Mater. 150 (2018) 182–194.
[35] R. Kobayashi, D. Giofré, T. Junge, M. Ceriotti, W.A. Curtin, Neural network potential for Al-Mg-Si alloys, Phys. Rev.Mater. 1 (2017), 053604.
[36] G. Imbalzano, A. Anelli, D. Giofré, S. Klees, J. Behler, M. Ceriotti, Automatic selection of atomic fingerprints and reference configurations for machine-learning potentials, J. Chem. Phys. 148 (2018) 241730.
[37] H. Zong, G. Pilania, X. Ding, G.J. Ackland, T. Lookman, Developing an interatomic potential for martensitic phase transformations in zirconium by machine learning, npj.Comput. Mater. 4 (2018) 48.
[38] E.V. Podryabinkin, A.V. Shapeev, Active learning of linearly parametrized interatomic potentials, Comput. Mater. Sci. 140 (2017) 171–180.
[39] J. Behler, M. Parrinello, Generalized neural-network representation of high-dimensional potential-energy surfaces, Phys. Rev. Lett. 98 (2007) 146401.
[40] A.P. Bartók, M.C. Payne, R. Kondor, G. Csányi, Gaussian approximation potentials: the accuracy of quantum mechanics, without the electrons, Phys. Rev. Lett. 104 (2010) 136403.
[41] K.T. Schütt, F. Arbabzadah, S. Chmiela, K.R. Müller, A. Tkatchenko, Quantum-chemical insights from deep tensor neural networks, Nat. Commun. 8 (2017) 13890.
[42] J.S. Smith, O. Isayev, A.E. Roitberg, ANI-1: an extensible neural network potential with DFT accuracy at force field computational cost, Chem. Sci. 8 (2017) 3192–3203.
[43] A.P. Thompson, L.P. Swiler, C.R. Trott, S.M. Foiles, G.J. Tucker, Spectral neighbor analysis method for automated generation of quantum-accurate interatomic potentials, J. Comput. Phys. 285 (2015) 316–330.
[44] S. Manzhos, R. Dawes, T. Carrington, Neural network-based approaches for building high dimensional and quantum dynamics-friendly potential energy surfaces, Int. J. Quantum Chem. 115 (2015) 1012–1020.
[45] T. Kostiuchenko, F. Körmann, J. Neugebauer, A. Shapeev, Impact of lattice relaxations on phase transitions in a high-entropy alloy studied by machine-learning potentials, npj.Comput. Mater. 5 (2019) 55.
[46] A.V. Shapeev, Applications of machine learning for representing interatomic interactions, in: Computational Materials Discovery, Royal Society of Chemistry, 2018, pp. 66–86.
[47] K. Gubaev, E.V. Podryabinkin, G.L. Hart, A.V. Shapeev, Accelerating high-throughput searches for new alloys with active learning of interatomic potentials, Comput. Mater. Sci. 156 (2019) 148–156.
[48] V. Botu, R. Batra, J. Chapman, R. Ramprasad, Machine learning force fields: construction, validation, and outlook, J. Phys. Chem. C 121 (2016) 511–522.
[49] T.D. Huan, R. Batra, J. Chapman, S. Krishnan, L. Chen, R. Ramprasad, A universal strategy for the creation of machine learning-based atomistic force fields, npj.Comput. Mater. 3 (2017) 37.
[50] J. Behler, Perspective: machine learning potentials for atomistic simulations, J. Chem. Phys. 145 (2016) 170901.
[51] I. Novoselov, A. Yanilkin, A. Shapeev, E. Podryabinkin, Moment tensor potentials as a promising tool to study diffusion processes, Comput. Mater. Sci. 164 (2019) 46–56.
[52] E.V. Podryabinkin, E.V. Tikhonov, A.V. Shapeev, A.R. Oganov, Accelerating crystal structure prediction by machine-learning interatomic potentials with active learning, Phys. Rev. B 99 (2019), 064114.
[53] I.S. Novikov, A.V. Shapeev, Improving accuracy of interatomic potentials: more physics or more data? A case study of silica, Mater. Today.Commun. 18 (2019) 74–80.
[54] I.S. Novikov, Y.V. Suleimanov, A.V. Shapeev, Automated calculation of thermal rate coefficients using ring polymer molecular dynamics and machine-learning interatomic potentials with active learning, Phys. Chem. Chem. Phys. 20 (2018) 29503–29512.
[55] A. Yeh, T. Tsao, Y. Chang, K. Chang, J. Yeh, M. Chiou, S. Jian, C. Kuo, W. Wang, H. Murakami, Developing new type of high temperature alloys–High Entropy Superalloys, Int. J. Metall. Mater.Eng. (2015) 2015.
[56] I. Tabakovic, V. Venkatasamy, Preparation of metastable CoFeNi alloys with ultra-high magnetic saturation (Bs = 2.4–2.59 T) by reverse pulse electrodeposition, J. Magn. Magn. Mater. 452 (2018) 306–314.
[57] Y. Zhang, T. Zuo, Y. Cheng, P.K. Liaw, High-entropy alloys with high saturation magnetization, Electrical Resistivity, and Malleability, Scientific Reports 3 (2013) 1455.
[58] H. Fu, H. Zhao, Y. Zhang, J. Xie, Enhancement of superelasticity in Fe-Ni-Co-based shape memory alloys by microstructure and texture control, Procedia.Eng 207 (2017) 1505–1510.
[59] P.E. Blöchl, Projector augmented-wave method, Phys. Rev. B 50 (1994) 17953–17979.
[60] G. Kresse, J. Furthmüller, Efficiency of ab-initio total energy calculations for metals and semiconductors using a plane-wave basis set, Comput. Mater. Sci. 6 (1996) 15–50.
[61] J.P. Perdew, K. Burke, M. Ernzerhof, Generalized gradient approximation made simple, Phys. Rev. Lett. 77 (1996) 3865.
[62] H.J. Monkhorst, J.D. Pack, Special points for Brillouin-zone integrations, Phys. Rev. B 13 (1976) 5188.
[63] M. Jamal, S.J. Asadabadi, I. Ahmad, H.R. Aliabad, Elastic constants of cubic crystals, Comput. Mater. Sci. 95 (2014) 592–599.
[64] S. Plimpton, Fast parallel algorithms for short-range molecular dynamics, J. Comput. Phys. 117 (1995) 1–19.
[65] S. Plimpton, P. Crozier, A. Thompson, LAMMPS-large-scale Atomic/molecular

Massively Parallel Simulator vol. 18, Sandia National Laboratories, 2007.
[66] S.M. Rassoulinejad-Mousavi, Y. Mao, Y. Zhang, Evaluation of copper, aluminum, and nickel interatomic potentials on predicting the elastic properties, J. Appl. Phys. 119 (2016) 244304.
[67] M. Jafary-Zadeh, Z.H. Aitken, R. Tavakoli, Y.-W. Zhang, On the controllability of phase formation in rapid solidification of high entropy alloys, J. Alloy. Comp. 748 (2018) 679–686.
[68] D.J. Evans, B.L. Holian, The nose–hoover thermostat, J. Chem. Phys. 83 (1985) 4069–4074.
[69] A. Stukowski, Visualization and analysis of atomistic simulation data with OVITO–the Open Visualization Tool, Model. Simul. Mater. Sci. Eng. 18 (2009), 015012.
[70] A.V. Shapeev, Moment tensor potentials: a class of systematically improvable interatomic potentials, Multiscale Model. Simul. 14 (2016) 1153–1173.
[71] K. Gubaev, E.V. Podryabinkin, A.V. Shapeev, Machine learning of molecular properties: locality and active learning, J. Chem. Phys. 148 (2018) 241727.
[72] R. Drautz, Atomic cluster expansion for accurate and transferable interatomic potentials, Phys. Rev. B 99 (2019), 014104.
[73] J.A. Zimmerman, H. Gao, F.F. Abraham, Generalized stacking fault energies for embedded atom FCC metals, Model. Simul. Mater. Sci. Eng. 8 (2000) 103.
[74] P. Branicio, J. Zhang, D. Srolovitz, Effect of strain on the stacking fault energy of copper: a first-principles study, Phys. Rev. B 88 (2013), 064104.
[75] R. Hill, The elastic behaviour of a crystalline aggregate, Proc. Phys. Soc. 65 (1952) 349.
[76] T. Teramoto, K. Yamada, R. Ito, K. Tanaka, Monocrystalline elastic constants and their temperature dependences for equi-atomic Cr-Mn-Fe-Co-Ni high-entropy alloy with the face-centered cubic structure, J. Alloy. Comp. 777 (2019) 1313–1318.
[77] W. Feng, Y. Qi, S. Wang, Effects of short-range order on the magnetic and mechanical properties of FeCoNi (AlSi) x high entropy alloys, Metals 7 (2017) 482.
[78] G. Alers, J. Neighbours, Crystal stability and elastic constants, J. Appl. Phys. 28 (1957) 1514, 1514.
[79] H. Zhang, X. Sun, S. Lu, Z. Dong, X. Ding, Y. Wang, L. Vitos, Elastic properties of $Al_xCrMnFeCoNi$ ($0\leq x\leq 5$) high-entropy alloys from ab initio theory, Acta Mater 155 (2018) 12–22.
[80] M. Jafary-Zadeh, R. Tavakoli, J. Koh, Z. Aitken, Y.-W. Zhang, Effect of chemical composition and affinity on the short-and medium-range order structures and mechanical properties of Zr-Ni-Al metallic glass, J. Non-Cryst. Solids 456 (2017) 68–75.
[81] G. Laplanche, P. Gadaud, C. Bärsch, K. Demtröder, C. Reinhart, J. Schreuer, E.P. George, Elastic moduli and thermal expansion coefficients of medium-entropy subsystems of the CrMnFeCoNi high-entropy alloy, J. Alloy. Comp. 746 (2018) 244–255.
[82] A. Stukowski, A. Arsenlis, On the elastic–plastic decomposition of crystal deformation at the atomic scale, Model. Simul. Mater. Sci. Eng. 20 (2012), 035012.
[83] Y. Cheng, E. Ma, Atomic-level structure and structure–property relationship in metallic glasses, Prog. Mater. Sci. 56 (2011) 379–473.
[84] C. Tang, C.H. Wong, Formation of chemical short range order and its influences on the dynamic/mechanical heterogeneity in amorphous Zr–Cu–Ag alloys: a molecular dynamics study, Intermetallics 70 (2016) 61–67.
[85] B. Feng, M. Widom, Elastic stability and lattice distortion of refractory high entropy alloys, Mater. Chem. Phys. 210 (2018) 309–314.
[86] Y. Tong, S. Zhao, K. Jin, H. Bei, J. Ko, Y. Zhang, F. Zhang, A comparison study of local lattice distortion in Ni80Pd20 binary alloy and FeCoNiCrPd high-entropy alloy, Scripta Mater. 156 (2018) 14–18.
[87] T. Egami, M. Ojha, O. Khorgolkhuu, D. Nicholson, G. Stocks, Local electronic effects and irradiation resistance in high-entropy alloys, JOM (J. Occup. Med.) 67 (2015) 2345–2349.
[88] M. Widom, W.P. Huhn, S. Maiti, W. Steurer, Hybrid Monte Carlo/molecular dynamics simulation of a refractory metal high entropy alloy, Metall. Mater. Trans. A 45 (2014) 196–200.
[89] Y. Ma, Q. Wang, C. Li, L.J. Santodonato, M. Feygenson, C. Dong, P.K. Liaw, Chemical short-range orders and the induced structural transition in high-entropy alloys, Scripta Mater. 144 (2018) 64–68.
[90] J. Ding, Q. Yu, M. Asta, R.O. Ritchie, Tunable stacking fault energies by tailoring local chemical order in CrCoNi medium-entropy alloys, Proc. Natl. Acad. Sci. Unit. States Am. 115 (2018) 8919–8924.
[91] Z. Liu, Y. Lei, C. Gray, G. Wang, Examination of solid-solution phase formation rules for high entropy alloys from atomistic Monte Carlo simulations, JOM 67 (2015) 2364–2374.
[92] P. Singh, A.V. Smirnov, D.D. Johnson, Atomic short-range order and incipient long-range order in high-entropy alloys, Phys. Rev. B 91 (2015) 224204.
[93] F. Zhang, S. Zhao, K. Jin, H. Xue, G. Velisa, H. Bei, R. Huang, J. Ko, D. Pagan, J. Neuefeind, Local structure and short-range order in a NiCoCr solid solution alloy, Phys. Rev. Lett. 118 (2017) 205501.
[94] J. Cowley, X-ray measurement of order in single crystals of Cu3Au, J. Appl. Phys. 21 (1950) 24–30.
[95] Z. Wu, H. Bei, G.M. Pharr, E.P. George, Temperature dependence of the mechanical properties of equiatomic solid solution alloys with face-centered cubic crystal structures, Acta Mater. 81 (2014) 428–441.
[96] J. Moon, M.J. Jang, J.W. Bae, D. Yim, J.M. Park, J. Lee, H.S. Kim, Mechanical behavior and solid solution strengthening model for face-centered cubic single crystalline and polycrystalline high-entropy alloys, Intermetallics 98 (2018) 89–94.
[97] F. Tian, L.K. Varga, J. Shen, L. Vitos, Calculating elastic constants in high-entropy alloys using the coherent potential approximation: current issues and errors, Comput. Mater. Sci. 111 (2016) 350–358.